Inorganic Chemistry
Article

Inorg. Chem. **2010**, *49*, 1947–1960 **1947**
DOI: 10.1021/ic9023426

Experimental and Theoretical Studies on Photophysical Properties: Tuning Redox-Active Amido-Tetrathiafulvalene Derivatives in Paramagnetic Coordination Complexes

Fabrice Pointillart,[†] Thomas Cauchy,[‡] Yann Le Gal,[†] Stéphane Golhen,[†] Olivier Cador,[†] and Lahcène Ouahab*[,†]

[†]*Organométalliques et Matériaux Moléculaires, and* [‡]*Chimie Théorique Inorganique, UMR 6226 CNRS-UR1 Sciences Chimiques de Rennes, Université de Rennes 1, 35042 Rennes Cedex, France*

Received December 2, 2009

Amido-5-pyrimidine (**1**), -4-pyridine (**2**), -2-pyrazine (**3**), -2-pyridine (**4**), and -2-pyridine-*N*-oxide (**5**) derivatives of TTF (TTF = tetrathiafulvalene) have been synthesized and characterized. The crystal structure of **1** has been resolved. Their capacities to coordinate paramagnetic transition metal have been explored. The following new molecular compounds have been synthesized and obtained as single crystals: $\{[Cu(hfac)_2(\mathbf{1})](H_2O)\}_2$ (**6**), *cis*-$[Mn(hfac)_2(\mathbf{2})_2](THF)_2$ (**7**), *trans*-$[Cu(hfac)_2(\mathbf{3})_2]$ (**8**), *trans*-$[Cu(hfac)_2(\mathbf{4})_2]$ (**9**), and *trans*-$[M(hfac)_2(\mathbf{5})_2]$ (M = Cu (**10**), Mn (**11**), Zn (**12**)). The crystal structures reveal that the nature of the coordinating substituent plays a fundamental role on the crystalline organization. Cyclic voltammetry measurements have been performed for all the species and they have permitted us to observe the redox activity of the free and linked donors. EPR measurements are in agreement with the solid-state structures. All the ligands and corresponding coordination complexes have been studied by UV−visible absorption spectroscopy. Gaussian deconvolutions have been performed to fit the experimental solid-state absorption curves. Molecular orbital diagram for ligands **4** and **5**; and their coordination complexes have been determined. The nature of the thirty to fifty low-lying monoelectronic transitions occurring in the TTF derivatives have been identified by TD-DFT calculations and their corresponding UV−visible absorption spectra have been simulated. Concerning the open-shell complexes, the excitations in the low energy region of their spectra have been calculated to determine the coordination effect on the TTF to acceptor transitions of the ligand fragments.

Introduction

The elaboration of multifunctional materials is a great challenge for the physicochemistry community. In particular, the synthesis of molecular materials exhibiting synergy between two or more properties is the source of intense investigations. Multiferroics and magnetochiral dichroism are important examples of such interactions.[1−3] Molecular compounds exhibiting electrical conductivity and magnetic interactions are currently of intensive studies. Two approaches are now well-known and explored. On one hand, the interactions between mobile electrons of the organic network (π-electrons) and localized electrons of paramagnetic transition metal (d-electrons) take place through space.[4] On the other hand, these interactions take place through covalent chemical bonds.[5] In the latter, two procedures are used to elaborate such materials: a"one-pot" procedure that consists of performing a galvanostatic oxidation from the starting metal salts and donors[6] and a "step-by-step" procedure

*To whom correspondence should be addressed. E-mail: Lahcene.Ouahab@univ-rennes1.fr.

(1) Spaldin, N. A.; Fiebig, M. *Science* **2005**, *309*, 391.
(2) Eerenstein, W.; Mathur, N. D.; Scott, J. F. *Nature* **2006**, *442*, 759.
(3) Train, C.; Gheorghe, R.; Krstic, V.; Chamoreau, L.-M.; Ovanesyan, N. S.; Rikken, G. L. J. A.; Gruselle, M.; Verdaguer, M. *Nat. Mater.* **2008**, *7*, 729.
(4) (a) Kobayashi, A.; Fujiwara, E.; Kobayashi, H. *Chem. Rev.* **2004**, *104*, 5243. (b) Enoki, T.; Miyasaki, A. *Chem. Rev.* **2004**, *104*, 5449. (c) Coronado, E.; Day, P. *Chem. Rev.* **2004**, *104*, 5419. (d) Ouahab, L.; Enoki, T. *Eur. J. Inorg. Chem.* **2004**, 933. (e) Fujiwara, H.; Wada, K.; Hiraoka, T.; Hayashi, T.; Sugimoto, T.; Nakazumi, H.; Yokogawa, K.; Teramura, M.; Yasuzuka, S.; Murata, K.; Mori, T. *J. Am. Chem. Soc.* **2005**, *127*, 14166. (f) Kato, R. *Bull. Chem. Soc. Jpn.* **2000**, *73*, 515.

(5) (a) Bouguessa, S.; Gouasmia, A. K.; Golhen, S.; Ouahab, L.; Fabre, J.-M. *Tetrahedron Lett.* **2003**, *44*, 9275. (b) Liu, S.-X.; Dolder, S.; Rusanov, E. B.; Stoecki-Evans, H.; Decurtins, S. *C. R. Chim.* **2003**, *6*, 657. (c) Liu, S.-X.; Dolder, S.; Pilkington, M.; Decurtins, S. *J. Org. Chem.* **2002**, *67*, 3160. (d) Jia, C.; Zhang, D.; Xu, Y.; Xu, W.; Hu, U.; Zhu, D. *Synth. Met.* **2003**, *132*, 249. (e) Becher, J.; Hazell, A.; McKenzie, C. J.; Vestergaard, C. *Polyhedron* **2000**, *19*, 665. (f) Devic, T.; Avarvari, N.; Batail, P. *Chem.—Eur. J.* **2004**, *10*, 3697. (g) Ota, A.; Ouahab, L.; Golhen, S.; Cador, O.; Yoshida, Y.; Saito, G. *New. J. Chem.* **2005**, *29*, 1135. (h) Liu, S.-X.; Dolder, S.; Franz, P.; Neels, A.; Stoeckli-Evans, H.; Decurtins, S. *Inorg. Chem.* **2003**, *42*, 4801. (i) Xue, H.; Tang, X.-J.; Wu, L.-Z.; Zhang, L.-P.; Tung, C.-H. *J. Org. Chem.* **2005**, *70*, 9727. (j) Benbellat, N.; Le Gal, Y.; Golhen, S.; Gouasmia, A.; Ouahab, L.; Fabre, J.-M. *Eur. J. Org. Chem.* **2006**, 4237. (k) Hervé, K.; Liu, S.-X.; Cador, O.; Golhen, S.; Le Gal, Y.; Bousseksou, A.; Stoeckli-Evans, H.; Decurtins, S.; Ouahab, L. *Eur. J. Inorg. Chem.* **2006**, 3498. (l) Massue, J.; Bellec, N.; Chopin, S.; Levillain, E.; Roisnel, T.; Clérac, R.; Lorcy, D. *Inorg. Chem.* **2005**, *44*, 8740. (m) Pellon, P.; Gachot, G.; Le Bris, J.; Marchin, S.; Carlier, R.; Lorcy, D. *Inorg. Chem.* **2003**, *42*, 2056. (n) Smucker, B. W.; Dunbar, K. R. J. *J. Chem. Soc., Dalton Trans.* **2000**, 1309. (o) Devic, T.; Batail, P.; Fourmigué, M.; Avarvari, N. *Inorg. Chem.* **2004**, *43*, 3136. (p) Iwahori, F.; Golhen, S.; Ouahab, L.; Carlier, R.; Sutter, J.-P. *Inorg. Chem.* **2001**, *40*, 6541. (q) Ouahab, L.; Iwahori, F.; Golhen, S.; Carlier, R.; Sutter, J.-P. *Synth. Met.* **2003**, *133−134*, 505. (r) Jia, C.; Liu, S.-X.; Ambrus, C.; Neels, A.; Labat, G.; Decurtins, S. *Inorg. Chem.* **2006**, *45*, 3152. (s) Ichikawa, S.; Kimura, S.; Mori, H.; Yoshida, G.; Tajima, H. *Inorg. Chem.* **2006**, *45*, 7575. (t) Wang, L.; Zhang, B.; Zhang, J. *Inorg. Chem.* **2006**, *45*, 6860. (u) Gavrilenko, K. S.; Le Gal, Y.; Cador, O.; Golhen, S.; Ouahab, L. *Chem. Commun.* **2007**, 280. (v) Pointillart, F.; Le Gal, Y.; Golhen, S.; Cador, O.; Ouahab, L. *Inorg. Chem.* **2008**, *47*, 9730.

Published on Web 01/21/2010

Scheme 1. Synthesis of $\{[Cu(hfac)_2(\mathbf{1})](H_2O)\}_2$ (**6**), *cis*-$[Mn(hfac)_2(\mathbf{2})_2](THF)_2$ (**7**), *trans*-$[Cu(hfac)_2(\mathbf{3})_2]$ (**8**), *trans*-$[Cu(hfac)_2(\mathbf{4})_2]$ (**9**), *trans*-$[Cu(hfac)_2(\mathbf{5})_2]$ (**10**), *trans*-$[Mn(hfac)_2(\mathbf{5})_2]$ (**11**), and *trans*-$[Zn(hfac)_2(\mathbf{5})_2]$ (**12**)

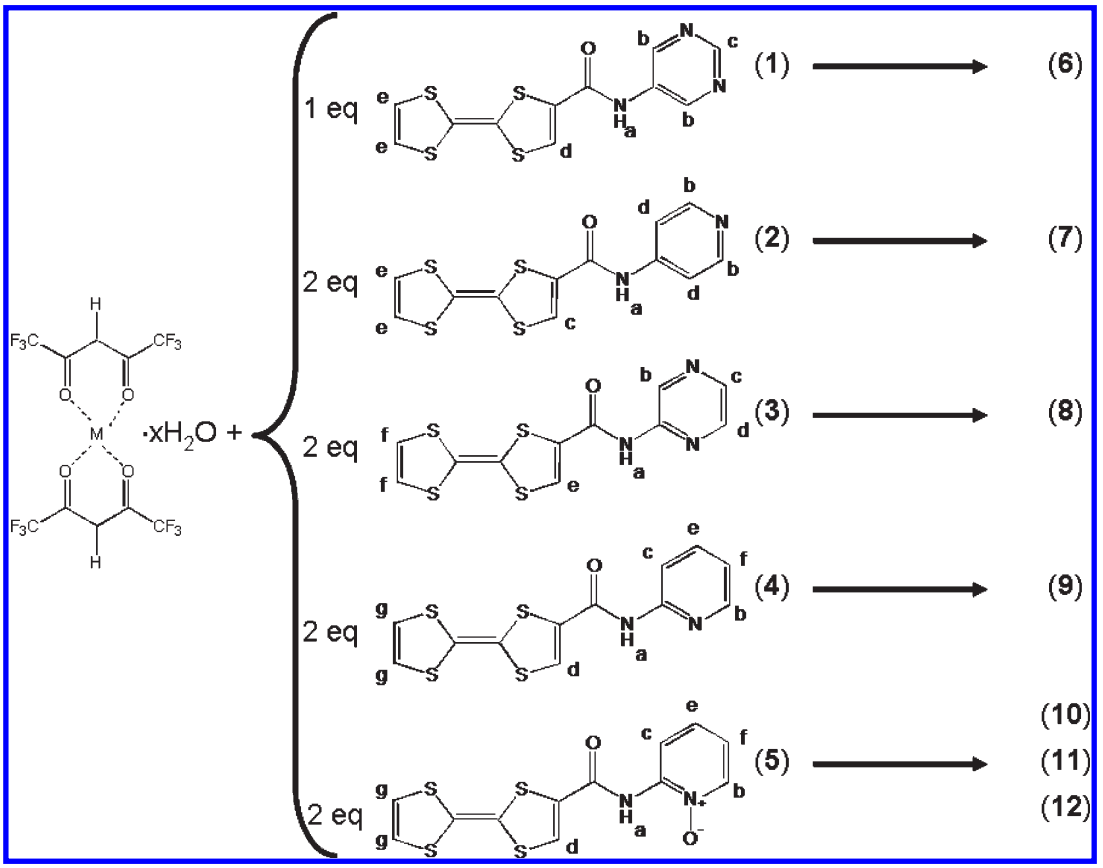

that consists first in the synthesis of a paramagnetic transition-metal-based coordination complex involving neutral redox-active TTF derivatives as ligand,[7] and then this complex is used as a molecular precursor to be submitted to the galvanostatic oxidation. The present work is devoted to this last procedure.

To elaborate a great diversity of redox-active molecular precursors, it is crucial to work from TTF-based ligands presenting an easy chemical synthetic procedure. A good choice is to put an amido-bridge to link the donor fragment and the coordinating substituent. The most studied ligands involving such bridge are the EDT-TTF (EDT = ethylenedithio) and BTM-TTF (BTM = bis(thiomethyl)) derivatives.[5f,8−10] They have been studied for their abilities to adopt a good crystalline organization through hydrogen bonds thanks to H-bond acceptor (carbonyl group) and H-bond donor (amido group).

To fill the challenge concerning the realization of molecular precursors before aiming multifunctional materials involving the direct interplay of magnetic and conducting properties, it is necessary to obtain the coordination of some amido-TTF derivatives to paramagnetic transition metal. Only one such paramagnetic precursor is reported in the literature.[10]

In this paper, we report the synthesis of five new amido-TTF ligands in which the TTF fragment is covalently linked to 2-pyridine, 4-pyridine, 2-pyrazine, 5-pyrimidine, and 2-pyridine-*N*-oxide through the amido-bridge (scheme 1). All these ligands are used to synthesize paramagnetic transition-metal-based coordination complexes. Ligands and complexes are fully characterized and their structural, photophysical and magnetic properties are reported. In particular, the absorption properties of some free donors and corresponding coordination complexes are discussed by a computational study based on the density functional theory (DFT).

Experimental Section

General Procedures and Materials. All other reagents were purchased from Aldrich Co. Ltd. and were used without further purification. All solvents were dried using standard procedures. 2-(Ethoxycarbonyl)tetrathiafulvalene (TTF-CO_2Et)[11] and 4-chlorocarbonyl-tetrathiafulvalene (TTF-COCl)[8,12,13] have been obtained from previously described methods which have been modified. Usually, the 2-carboxytetrathiafulvalene (TTF-CO_2H)

(6) (a) Ichikawa, S.; Kimura, S.; Takahashi, K.; Mori, H.; Yoshida, G.; Manabe, Y.; Matsuda, M.; Tajima, H.; Yamaura, J.-I. *Inorg. Chem.* **2008**, *47*, 4140. (b) Lu, W.; Zhang, Y.; Dai, J.; Zhu, Q.-Y.; Bian, G.-Q.; Zhang, D.-Q. *Eur. J. Inorg. Chem.* **2006**, 1629.

(7) (a) Avarvari, N.; Fourmigué, M. *Chem. Commun.* **2004**, 1300. (b) Kubo, K.; Nakano, A.; Tamura, M.; Matsubayashi, G. *Eur. J. Inorg. Chem.* **2008**, 5495. (c) Tanaka, H.; Kobayashi, H.; Kobayashi, A. *J. Am. Chem. Soc.* **2002**, *124*, 10002. (d) Liu, S.-X.; Ambrus, C.; Dolder, S.; Neels, A.; Decurtins, S. *Inorg. Chem.* **2006**, *45*, 9622. (e) Hervé, K.; Le Gal, Y.; Ouahab, L.; Golhen, S.; Cador, O. *Synth. Met.* **2005**, *153*, 461. (f) Setifi, F.; Ouahab, L.; Golhen, S.; Yoshida, Y.; Saito, G. *Inorg. Chem.* **2003**, *42*, 1791.

(8) Heuzé, K.; Fourmigué, M.; Batail, P. *J. Mater. Chem.* **1999**, *9*, 2973.

(9) Baudron, S. A.; Avarvari, N.; Batail, P.; Coulon, C.; Clérac, R.; Canadell, E.; Auban-Senzier, P. *J. Am. Chem. Soc.* **2003**, *125*, 11583.

(10) Devic, T.; Rondeau, D.; Sahin, Y.; Levillain, E.; Clérac, R.; Batail, P.; Avarvari, N. *Dalton Trans.* **2006**, 1331.

(11) Green, D. C. *J. Org. Chem.* **1979**, *44*, 1476.

(12) Chesney, A.; Bryce, M. R. *Tetrahedron: Asymmetry* **1996**, *7*, 3247.

(13) Panetta, C. A.; Baghdachi, J.; Metzger, R. *Mol. Cryst. Liq. Cryst.* **1984**, *107*, 103.

compound is obtained by the reaction of CO_2 gas with the tetrathiafulvalenyllithium.[11] We have chosen to modify the method described for the synthesis of other chlorocarbonyl-tetrathiafulvalene derivatives.[5f,8,14] The precursors $M(hfac)_2 \cdot xH_2O$ (M = Mn, Cu, and Zn) have been synthesized following the previously reported methods.[15]

Synthesis of Carbomoytetrathiafulvalene Ligands 1−5. 2-(Ethoxycarbonyl)tetrathiafulvalene (TTF-CO_2Et). Under an argon atmosphere, a slurry of 9.8 mmol of tetrathiafulvalenyl-lithium[16] (0.01 mmol) at −78 °C was slowly added over 1 h via a Teflon tube inserted through a septum cap into a Et_2O solution (200 mL) at −78 °C containing 4.8 mL of ethylchloroformate (0.05 mmol). The resulting red mixture was allowed to warm to room temperature and washed with 200 mL of water, and the organic phase was dried over $MgSO_4$. The solvent was removed under a vacuum, leading to an oil that was purified by silica column chromatography (eluent CH_2Cl_2/pentane 1:1). Pure crystalline orange TTF-CO_2Et was obtained after recrystallization in CH_2Cl_2/hexane. Yield: 865 mg, (32%). I.R. 1691, 1532, 1286, 1062, 719 cm^{-1}. Anal. Calcd (%) for $C_9H_8O_2S_4$: C, 39.10; H, 2.89. Found: C, 39.19; H, 2.93.

2-Carboxytetrathiafulvalene (TTF-CO_2H). A solution of THF (40 mL) containing 170 mg of TTF-CO_2Et (0.6 mmol) and an aqueous solution of 1 M LiOH (3 mL, 3 mmol) were heated to reflux during 3 h. After this delay, the THF was removed under a vacuum and the residual oil was dissolved in 30 mL of water. The aqueous solution was neutralized by addition of 1 M HCl, leading to the precipitation of a red solid that was filtered, washed with a lot of water, and dried. Yield: 140 mg, (93%). I.R. 1650, 1559, 1297, 732 cm^{-1}. Anal. Calcd (%) for $C_7H_4O_2S_4$: C, 33.85; H, 1.68. Found: C, 34.09; H, 1.63.

4-Chlorocarbonyl-tetrathiafulvalene (TTF-COCl). One-hundred-thirty-five milligrams of TTF-COOH (0.54 mmol) was dissolved in 21 mL of THF and heated at 45 °C. The addition of 0.20 mL of oxalyl chloride (2.16 mmol) following by 0.5 μL of pyridyl to the hot solution provokes a fast change of color from red to purple. After 4 h, the solution was concentrated 5 times under a vacuum (4 mL) and the dark purple solid of TTF-COCl was obtained by addition of hexane. Yield: 115 mg, (80%). I.R. 1699, 1530, 1507, 1151, 756 cm^{-1}. Anal. Calcd (%) for $C_7H_3OClS_4$: C, 31.52; H, 1.13. Found: C, 31.39; H, 1.23.

5-Pyrimidine-carbamoyltetrathiafulvalene (1). One-hundred-six milligrams of TTF-COCl (0.4 mmol) in THF (10 mL) was added slowly to a solution of 5-aminopyrimidine (190 mg, 2 mmol) in THF (5 mL) under magnetic stirring and argon atmosphere. During the addition, a brown solid appears. At the end of the addition, the THF was removed under vacuum and the residual solid washed 3−4 times with 20 mL of water to remove the excess of 5-aminopyrimidine. A brown solid was obtained after filtration which was purified by silica column chromatography (eluent THF) leading to an orange-brown solid of **1**. Compound **1** was recovered as orange crystals, suitable for a single-crystal X-ray analysis, after slow evaporation of a saturated THF solution of **1**. Yield: 109 mg, (84%). ^{1}H NMR (d6-DMSO): δ = 10.80 (*s*, 1H; H_a), 9.06 (*s*, 2H, H_b), 8.95 (*s*, 1H, H_c), 7.99 (*s*, 1H, H_d), 6.79 (*s*, 2H, H_e); I.R. 3063, 3024, 2963, 2854, 1654, 1595, 1430, 1295, 1261, 798, 659 cm^{-1}.

4-Pyridyl-carbomoyltetrathiafulvalene (2). This ligand was synthesized by a similar procedure to that used for **1** starting from 80 mg of TTF-COCl (0.3 mmol) and 4-aminopyridine (140 mg, 1.5 mmol). Pure red-brown solid of **2** was obtained after a silica column chromatography (eluent THF). Yield: 60 mg (62%). ^{1}H NMR (d6-DMSO): δ = 10.59 (*s*, 1H; H_a), 8.49 (*d*, *J* = 6.0 Hz, 2H, H_b), 7.92 (*s*, 1H, H_c), 7.63 (*d*, *J* = 6.0 Hz, 2H, H_d), 6.79 (*s*, 2H, H_e); I.R. 3070, 3027, 2929, 1647, 1519, 1466, 1415, 1333, 1291, 820, 652 cm^{-1}.

2-Pyrazine-carbomoyltetrathiafulvalene (3). This ligand was synthesized by a similar procedure to that used for **1** starting from 54 mg of TTF-COCl (0.2 mmol) in THF (7.5 mL) and 2-aminopyrazine (76 mg, 0.4 mmol). Pure red-brown solid of **3** was obtained after a silica column chromatography (eluent THF). Yield: 40 mg (62%). ^{1}H NMR (d6-DMSO): δ = 11.28 (*s*, 1H; H_a), 9.27 (*s*, 1H, H_b), 8.46 (*d*, *J* = 8.0 Hz, 2H, H_c, H_d), 8.15 (*s*, 1H, H_e), 6.79 (*s*, 2H, H_f); I.R. 3070, 3027, 2921, 1653, 1533, 1463, 1411, 1294, 788, 718 cm^{-1}.

2-Pyridyl-carbomoyltetrathiafulvalene (4). This ligand was synthesized by a similar procedure to that used for **1** starting from 80 mg of TTF-COCl (0.3 mmol) and 2-aminopyridine (140 mg, 1.5 mmol). Pure orange solid of **4** was obtained after a silica column chromatography (eluent THF/CH_3CN 1:1). Yield: 50 mg (52%). ^{1}H NMR (d_6-DMSO): δ = 10.96 (*s*, 1H; H_a), 8.40 (*d*, *J* = 4.0 Hz, 1H, H_b), 8.11 (*brs*, 1H, H_c), 7.99 (*s*, 1H, H_d), 7.85 (*m*, 1H, H_e), 7.20 (*m*, 1H, H_f) 6.78 (*s*, 2H, H_g); I.R. 3376, 3067, 3027, 1646, 1576, 1535, 1433, 1307, 1224, 793, 650 cm^{-1}.

2-Pyridyl-*N*-oxide-carbomoyltetrathiafulvalene (5). This ligand was synthesized by a similar procedure to that used for **1** starting from 318 mg of TTF-COCl (1.2 mmol) and 2-aminopyridine-*N*-oxide[17] (600 mg, 5.5 mmol). Pure red-brown solid of **5** was obtained after remove the excess of 2-aminopyridine-*N*-oxide with water (5 × 20 mL). Yield: 310 mg (76%). ^{1}H NMR (d6-DMSO): δ = 10.64 (*s*, 1H; H_a), 8.49 (*d*, *J* = 6.0 Hz, 1H, H_b), 8.13 (*brs*, 1H, H_c), 7.90 (*s*, 1H, H_d), 7.71 (*m*, 1H, H_e), 7.24 (*m*, 1H, H_f) 6.80 (*s*, 2H, H_g); I.R. 3067, 3027, 2925, 1698, 1608, 1570, 1514, 1429, 1309, 1262, 1206, 799, 755, 718, 638 cm^{-1}.

Synthesis of Complexes 6−12. **{[Cu(hfac)$_2$(1)]·H_2O}$_2$ (6).** A solution of heptane (10 mL) containing 10.4 mg of $Cu(hfac)_2 \cdot 2H_2O$ (0.02 mmol) was concentrated under reflux until a volume of 5 mL. The solution was then cooled to 65 °C and a solution of CH_2Cl_2 (8 mL) containing 6.5 mg of **1** (0.02 mmol) was added in one time. A weak shift to darker red color is observed. The mixture was stirred at room temperature for 20 min. Slow evaporation of the resulting solution in the dark has led to orange-brown twin platelets of **6**, which are suitable for a single-crystal X-ray diffraction. Yield: 24 mg (73%). I.R. 2925, 2854, 1650, 1538, 1465, 1439, 1340, 1259, 1210, 1146, 803, 708, 671, 591 cm^{-1}.

***cis*-[Mn(hfac)$_2$(2)$_2$]·(THF)$_2$ (7).** This complex was synthesized by a similar procedure to that used for **6** starting from 10.5 mg of $Mn(hfac)_2 \cdot 3H_2O$ (0.02 mmol) and 13.0 mg of **2** (0.04 mmol). A weak shift to darker red color is observed. Recrystallization from a mixture of CH_2Cl_2/hexane (1:1 in volume) with two drops of THF, has given orange needles of **7**, suitable for a single-crystal X-ray diffraction. Yield: 9 mg (36%). I.R. 3190, 3116, 3010, 2925, 2852, 1656, 1603, 1532, 1508, 1495, 1321, 1291, 1256, 1203, 1144, 832, 798, 727, 664, 581 cm^{-1}.

***trans*-[Cu(hfac)$_2$(3)$_2$] (8).** A solution of CH_2Cl_2 (5 mL) containing 13.0 mg of **3** (0.04 mmol) was added at room temperature to a solution of CH_2Cl_2 (5 mL) containing 10.3 mg of $Cu(hfac)_2 \cdot 2H_2O$ (0.02 mmol). A weak shift to darker red color is observed. After 15 min of stirring, the solution was put in a closed flask and 15 mL of hexane were layered. After two days of diffusion, small red needles of **8**, suitable for a single-crystal X-ray diffraction, were obtained. Yield: 6 mg (27%). I.R. 3070, 2923, 2853, 1675, 1645, 1617, 1575, 1531, 1472, 1433, 1308, 1257, 1218, 1146, 773, 675, 649, 595 cm^{-1}.

***trans*-[Cu(hfac)$_2$(4)$_2$] (9).** This complex was synthesized by a similar procedure to that used for **6** starting from 10.4 mg of $Cu(hfac)_2 \cdot 2H_2O$ (0.02 mmol) and 13.0 mg of **4** (0.04 mmol).

(14) Zhao, B.-T.; Blesa, M.-J.; Le Derf, F.; Canevet, D.; Benhaoua, C.; Mazari, M.; Allain, M.; Sallé, M. *Tetrahedron* **2007**, *63*, 10768.
(15) Richardson, M. F.; Wagner, W. F.; Sands, D. E. *J. Inorg. Nucl. Chem.* **1968**, *30*, 1275.
(16) Garin, J.; Orduna, J.; Uriel, S.; Moore, A. J.; Bryce, M. R.; Wegener, S.; Yufit, D. S.; Howard, J. A. K. *Synthesis* **1994**, 489.
(17) Abramovitch, A. R.; Cue, B. W., Jr. *J. Am. Chem. Soc.* **1976**, *17*, 1478.

Table 1. X-ray Crystallographic Data

	TTF-CONH-5-Pym **1**	{[Cu(hfac)$_2$(**1**)](H$_2$O)}$_2$**6**	*cis*-[Mn(hfac)$_2$(**2**)$_2$](THF)$_2$**7**	*trans*-[Cu(hfac)$_2$(**3**)$_2$] **8**
formula	$C_{11}H_7N_3OS_4$	$C_{42}H_{22}N_6O_{12}S_8F_{24}Cu_2$	$C_{42}H_{34}N_4O_8S_8F_{12}Mn$	$C_{32}H_{16}N_6O_6S_8F_{12}Cu$
M (g mol^{-1})	325.4	1642.2	1256.1	1128.5
cryst syst	monoclinic	triclinic	monoclinic	triclinic
space group	$P21/c$ (No. 14)	$P\bar{1}$ (No. 2)	$C2/c$ (No. 15)	$P\bar{1}$ (No. 2)
a (Å)	8.365(2) Å	9.548(5) Å	16.9912(5) Å	9.0330(10) Å
b (Å)	13.473(3) Å	14.816(5) Å	10.5910(4) Å	9.7994(17) Å
c (Å)	11.756(2) Å	21.493(5) Å	30.1362(15) Å	12.562(2) Å
α (deg)		94.972(5)		90.436(5)
β (deg)	100.431(10)	94.610(5)	91.067(2)	111.043(8)
γ (deg)		93.274(5)		99.410(8)
V (Å^3)	1303.1(4)	3013.0(2)	5422.2(4)	1021.2(3)
cell formula units	$Z = 4$	$Z = 2$	$Z = 4$	$Z = 1$
T (K)	293 (2)	293 (2)	293 (2)	293 (2)
diffraction refln	$4.64° \le 2\theta \le 55.20°$	$4.54° \le 2\theta \le 53.48°$	$6.06° \le 2\theta \le 52.76°$	$5.66° \le 2\theta \le 52.82°$
ρ_{calcd} (g cm^{-3})	1.659	1.810	1.546	1.835
μ (mm^{-1})	0.721	1.119	0.645	1.052
no. of reflns	5420	22554	15899	6258
no. of independent reflns	3836	12717	5547	3867
$F_o^2 > 2\sigma(F_o)^2$	2927	7958	2282	2110
no. of variables	172	955	393	295
R_1, wR_2	0.0675, 0.1067	0.0628, 0.1680	0.0583, 0.1533	0.0594, 0.1193

	trans-[Cu(hfac)$_2$(**4**)$_2$] **9**	*trans*-[Cu(hfac)$_2$(**5**)$_2$] **10**	*trans*-[Mn(hfac)$_2$(**5**)$_2$] **11**	*trans*-[Zn(hfac)$_2$(**5**)$_2$] **12**
formula	$C_{34}H_{18}N_4O_6S_8F_{12}Cu$	$C_{34}H_{18}N_4O_8S_8F_{12}Cu$	$C_{34}H_{18}N_4O_8S_8F_{12}Mn$	$C_{34}H_{18}N_4O_8S_8F_{12}Zn$
M (g mol^{-1})	1126.5	1158.5	1149.9	1160.4
cryst syst	triclinic	monoclinic	monoclinic	monoclinic
space group	$P\bar{1}$ (No. 2)	$P2_1/n$ (No. 14)	$P2_1/n$ (No. 14)	$P2_1/n$ (No. 14)
a (Å)	9.187(1)	11.150(5)	11.366(5)	11.2437(2)
b (Å)	9.910(1)	11.061(5)	11.391(5)	11.1538(3)
c (Å)	12.604(1) Å	18.417(5) Å	17.989(4) Å	18.3042(5) Å
α (deg)	110.193(10)			
β (deg)	101.977(10)	103.818(5)	104.560(6)	104.175(2)
γ (deg)	101.977(10)			
V (Å^3)	1050.9(2)	2205.6(16)	2254.2(15)	2225.64(9)
cell formula units	$Z = 1$	$Z = 2$	$Z = 2$	$Z = 2$
T (K)	293 (2)	293 (2)	293 (2)	293 (2)
diffraction refln	$13.60° \le 2\theta \le 55.00°$	$3.90° \le 2\theta \le 55.00°$	$4.68° \le 2\theta \le 57.38°$	$3.88° \le 2\theta \le 54.94°$
ρ_{calcd} (g cm^{-3})	1.780	1.744	1.694	1.732
μ (mm^{-1})	1.021	0.979	0.766	1.031
no. of reflns	8246	9765	11229	9884
no. of independent reflns	4723	5064	5800	5102
$F_o^2 > 2\sigma(F_o)^2$	2647	3473	3457	3526
no. of variables	323	360	360	360
R_1, wR_2	0.0565, 0.1351	0.0409, 0.1061	0.0423, 0.1002	0.0384, 0.0932

A weak shift to darker red color is observed. Slow evaporation of the CH_2Cl_2/heptane solution in the dark, has given orange needles of **9**, suitable for a single-crystal X-ray diffraction. Yield: 11 mg (49%). I.R. 3070, 2923, 2853, 1675, 1645, 1617, 1575, 1531, 1472, 1433, 1308, 1257, 1218, 1146, 773, 675, 649, 595 cm^{-1}.

***trans*-[Cu(hfac)$_2$(5)$_2$] (10).** This complex was synthesized by a similar procedure to that used for **9** starting from 10.4 mg of Cu(hfac)$_2\cdot 2H_2O$ (0.02 mmol) and 13.5 mg of **5** (0.04 mmol). A change of color from red to dark red is observed. Slow evaporation of the CH_2Cl_2/heptane solution in the dark, has given dark purple crystals of **10**, suitable for a single-crystal X-ray diffraction. Yield: 16 mg (69%). I.R. 3295, 3070, 2923, 1679, 1651, 1617, 1579, 1514, 1432, 1321, 1256, 1200, 1143, 831, 793, 763, 663 cm^{-1}.

***trans*-[Mn(hfac)$_2$(5)$_2$] (11).** This complex was synthesized by a similar procedure to that used for **10** starting from 10.5 mg of Mn(hfac)$_2\cdot 3H_2O$ (0.02 mmol) and 13.5 mg of **5** (0.04 mmol). A change of color from red to dark red is observed. Slow evaporation of the CH_2Cl_2/heptane solution in the dark, has given red block-shaped crystals of **11**, suitable for a single-crystal X-ray diffraction. Yield: 10 mg (43%). I.R. 3372, 3071, 2923, 1683, 1653, 1575, 1530, 1469, 1430, 1258, 1215, 1145, 788, 671 cm^{-1}.

***trans*-[Zn(hfac)$_2$(5)$_2$] (12).** This complex was synthesized by a similar procedure to that used for **10** starting from 10.3 mg of Zn(hfac)$_2\cdot 2H_2O$ (0.02 mmol) and 13.5 mg of **5** (0.04 mmol). A red solid appeared after 5 min and was dissolved by addition of 1.5 mL of THF. A change of color from red to dark red is observed. Slow evaporation of the THF/CH_2Cl_2/heptane solution in the dark, has given red block-shaped crystals of **12**, suitable for a single-crystal X-ray diffraction. Yield: 12 mg (52%). I.R. 3370, 3070, 2920, 1678, 1652, 1574, 1533, 1471, 1432, 1258, 1209, 1144, 830, 790, 759, 671 cm^{-1}.

Crystallography. Single crystals were mounted on a Nonius four circle diffractometer equipped with a CCD camera and a graphite monochromated MoK_α radiation source ($\lambda = 0.71073$ Å), from the Centre de Diffractométrie (CDFIX), Université de Rennes 1, France. Data were collected at 293 K. Structures were solved with direct methods using the SIR-97 program and refined with a full matrix least-squares method on F^2 using the SHELXL-97 program.[18] Crystallographic data are summarized in Table 1. Complete crystal structure results as CIF files including bond lengths, angles, and atomic coordinates are deposited as Supporting Information.

Physical Measurements. All the physical measurements have been realized on crunched or dissolved single crystals of related compounds. ^{1}H NMR was recorded on a Bruker AC 300P

(18) Sheldrick, G. M.; *SHELXL-97, Program for Refinement of Crystal Structures*; University of Göttingen: Göttingen, Germany, 1997.

Table 2. Selected Bond Lengths (Å) and Angles (deg) for **9** and **10**

9		**10**	
Cu1−O2	1.957(3)	Cu1−O2	1.981(2)
Cu1−O3	1.953(3)	Cu1−O3	2.014(2)
Cu1−N2	2.432(4)	Cu1−O4	2.205(2)
C3−C4	1.340(6)	C3−C4	1.342(4)
C7−O1	1.212(6)	C7−O1	1.214(3)
Cu1−Cu1	9.187(1)	Cu1−O2−N2	119.19(15)
		Cu1−Cu1	11.043(35)

spectrometer. Chemical shifts are reported in parts per million referenced to TMS for ^{1}H NMR. Cyclic voltametry was carried out in CH_2Cl_2 solution, containing 0.1 M $N(C_4H_9)_4PF_6$ as supporting electrolyte. Voltamograms were recorded at 100 mV s^{-1} at a platinum disk electrode. The potentials were measured versus a saturated calomel electrode (SCE) (Table 2). Infrared (IR) spectra were measured using the KBr disk method on Perkin-Elmer 1600 Series FT-IR (resolution 4 cm^{-1}). Absorption spectra were recorded using the KBr disk method on a Varian Cary 5000 UV−visible-NIR spectrometer equipped with an integration sphere. EPR spectra were recorded down to 67 K for powder sample of **6** and **11** with a BRUKER EMX X-band ESR spectrometer equipped with an OXFORD cryostat.

Computational Details. The UV−visible absorption spectra of TTF derivatives **1**, **4** and **5**, and complexes **9** and **10** have been calculated. At first, a full geometry optimization of all the TTF derivatives has been carried out using density functional theory (DFT) methods, whereas the solid state geometry has been used with a single-point calculation for complexes **9** and **10** with the same method. All calculations were performed with the hybrid functional adaptation of PBE[19] (usually referred as PBE0) as implemented on the Gaussian03 program.[20] Tests on the ligands with the GGA functional BP86[21] have led to very similar results. To manage calculation on the whole complexes **9** and **10**, we used a double-ζ quality basis set proposed by Weigend et al. with polarization functions for all atoms.[22] The differences with a triple-ζ quality basis set was probed on the ligands and they are meaningless. The first monoelectronic excitations (50 for the ligands and 30 for the complexes) were then computed using a time-dependent density functional theory (TD-DFT) procedure with the same program, functional, and basis set as the first step.

Results and Discussion

Synthesis. To study a great diversity of carbomoyl-TTF based neutral precursors, we need a library of different carbomoyl-TTF. Thus, substituents involving nitrogenated monochelate site of coordination as 2-pyridine and 4-pyridine, oxygenated monochelate site of coordination as 2-pyridine-*N*-oxide and nitrogenated bis-(monochelate) site of coordination as 2-pyrazine and 5-pyrimidine are used. In this work, we have only studied the zero-dimensional structures. Nevertheless, the two ligands 5-pyrimidine-carbamoyltetrathiafulvalene (**1**) and 2-pyrazine-carbomoyltetrathiafulvalene (**3**) are suitable to build monodimensional structures. It can be noticed that the ligand 2-pyridyl-*N*-oxide-carbomoyltetrathiafulvalene (**5**) permits us to increase the chance of coordination of the oxophile metallic ions as Mn(II) and Zn(II).

The five TTF derivatives are synthesized by the reaction between 4-chlorocarbonyl-tetrathiafulvalene[8,12,13] and an excess of corresponding amino-substituent.[5f,8] The molecular complexes are obtained by the reaction between the appropriated carbomoyl-TTF ligand and the bis(1,1,1,5,5,5-hexafluoroacethylacetonate)metal(II) in noncoordinated solvents (Scheme 1).

Crystal Structures. One ligand (**1**) and seven mononuclear complexes (**6**−**12**) involving the synthesized donors are crystallized. The crystallographic data for all X-ray structures are given in Table 1. One of the aims of this paper is the observation of the coordination effect of a metallic center on the absorption properties of the TTF ligand. To perform that, we need two coordination complexes involving similar metallic center but with diverse coordination strength. The complexes **9** and **10** involved the same Cu(II) ion but the different direction of the Jahn teller axis should alter the coordination effects. For this reason, we have focused our attention on the complexes **9** and **10** and their structural descriptions are given in the main text. Nevertheless, the structural descriptions for all the other compounds are also investigated and given in the Supporting Information (Table S1 and Figure S1−11).

Crystal Structure of *trans*-[Cu(hfac)$_2$(4)$_2$] (9) and *trans*-[Cu(hfac)$_2$(5)$_2$] (10). Compound **9** is isostructural with **8**. It crystallizes in the triclinic P-1 (N°2) space group (Table 1). An ORTEP[23] view of one molecule of **9** is shown in Figure 1. The asymmetric unit is composed of one ligand **4** and one ligand $hfac^-$, both coordinated to a divalent Cu(II) that is localized in the inversion center. The full molecule **9** is generated by this element of symmetry. The linked ligands **4** are planar and the central C=C (1.343(5) Å) bond length confirms their neutral form in the complex **9**. The $hfac^-$ anions are linked to the copper center through the oxygen atoms (Cu1−O2 = 1.957(3) Å and Cu1−O3 = 1.953(3) Å (Table 2)), forming the equatorial plane, whereas ligands **4** are linked in axial positions through the N2 nitrogen atoms of the pyridine moiety (Figure 1), which is the Jahn−Teller elongation with Cu1−N2 bond lengths (2.432(4) Å). The copper ion adopts a strongly elongated octahedral geometry. Such coordination mode can be explained by the following reason: the N2 nitrogen atom has a greater acceptor character than the N3 one and so the coordination is favored with this atom. But this coordination imposes a long distance even for a Jahn−Teller elongation because of the steric hindrance of the amido-TTF group. This

(19) (a) Perdew, J. P.; Burke, K.; Ernzerhof, M. *Phys. Rev. Lett*. **1996**, *77*, 3865. (b) Adamo, C.; Barone, V. *J. Chem. Phys*. **1999**, *110*, 6158.

(20) Frisch, M. J.; Trucks, G. W.; Schlegel, H. B.; Scuseria, G. E.; Robb, M. A.; Cheeseman, J. R.; Montgomery, J. A.; Vreven, T.; Kudin, K. N.; Burant, J. C.; Millam, J. M.; Iyengar, S. S.; Tomasi, J.; Barone, V.; Mennucci, B.; Cossi, M.; Scalmani, G.; Rega, N.; Petersson, G. A.; Nakatsuji, H.; Hada, M.; Ehara, M.; Toyota, K.; Fukuda, R.; Hasegawa, J.; Ishida, H.; Nakajima, T.; Honda, Y.; Kitao, O.; Nakai, H.; Klene, M.; Li, X.; Knox, J. E.; Hratchian, H. P.; Cross, J. B.; Adamo, C.; Jaramillo, J.; Gomperts, R.; Stratmann, R. E.; Yazyev, O.; Austin, A. J.; Cammi, R.; Pomelli, C.; Ochterski, J.; Ayala, P. Y.; Morokuma, K.; Voth, G. A.; Salvador, P.; Dannenberg, J. J.; Zakrzewski, V. G.; Dapprich, S.; Daniels, A. D.; Strain, M. C.; Farkas, O.; Malick, O. K.; Rabuck, A. D.; Raghavachari, K.; Foresman, J. B.; Ortiz, J. V.; Cui, Q.; Baboul, A. G.; Clifford, S.; Cioslowski, J.; Stefanov, B. B.; Liu, G.; Liashenko, A.; Piskorz, P.; Komaromi, I.; Martin, R. L.; Fox, D. J.; Keith, T.; Al-Laham, M. A.; Peng, C. Y.; Nanayakkara, A.; Challacombe, M.; Gill, P. M. W.; Johnson, B.; Chen, W.; Wong, M. W.; Gonzalez, C.; Pople, J. A. *Gaussian 03* (*revision D.02*).; Gaussian, Inc.: Pittsburgh, PA, 2003.

(21) (a) Becke, A. D. *Phys. Rev. A* **1988**, *38*, 3098. (b) Perdew, J. P. *Phys. Rev. B* **1986**, *33*, 8822.

(22) Weigend, F.; Ahlrichs, R. *Phys. Chem. Chem. Phys*. **2005**, *7*, 3297.

(23) Johnson, C. K. *ORTEP, Report ORNL-5138*; Oak Ridge National Laboratory: Oak Ridge, TN, 1976.

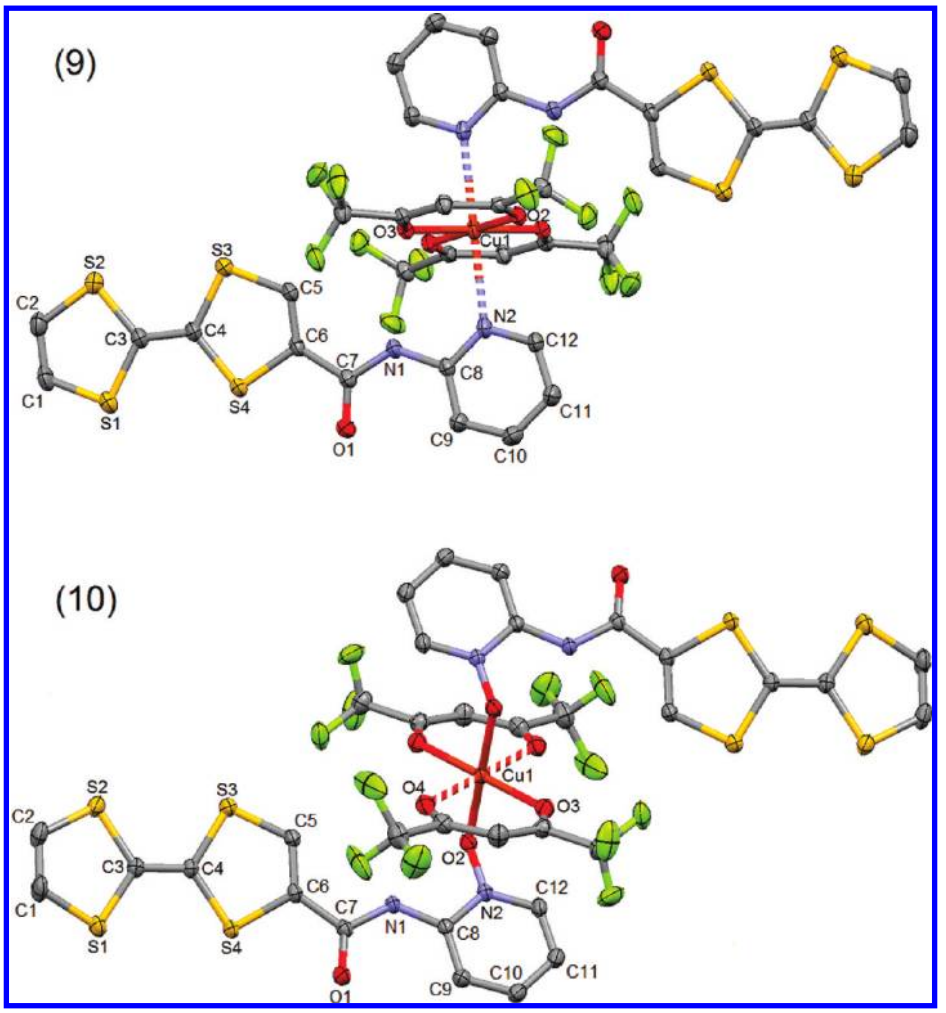

Figure 1. ORTEP view of *trans*-[Cu(hfac)$_2$(**4**)$_2$] (**9**) (top) and *trans*-[Cu(hfac)$_2$(**5**)$_2$] (**10**) (bottom) with thermal ellipsoids at the 30% probability level. Hydrogen atoms are omitted for clarity. Dashed bonds represent the long Cu-X distances along the Jahn−Teller axis.

observation is supported by the fact that the attempts to coordinate metal ions like Mn(II) and Zn(II) have failed because these ions can not adopt such distorted geometry. In contrary, in the complexes involving imino-TTF,[24] the divalent Cu(II) is coordinated to the N3 nitrogen atoms because the coordination to the N2 atom imposes the participation of the imino-nitrogen atom leading to a *cis*-conformation of the ligand,[25] which is less favorable than the *trans*-one for a Cu(II) ion.

In the solid, the complexes **9** interact one with the others through S···S contacts and $\pi\cdots\pi$ interactions. The crystal structure permits to identify the $\pi\cdots\pi$ stack between the aromatic pyridine rings along the *b*-axis (Figure 2a). The shortest distance between the pyridine moieties is equal to 3.631(9) Å. Figure S10a depicts the packing of molecules view in the plane (112), some of them are shown as capped stick. Between these molecules, S···S intermolecular contacts are observed (S2···S2 = 3.864(4) Å) but they are longer than the sum of van der Waals radius. The strong interactions take place along the [$\bar{1}$12] direction; a detail of these short S···S contacts (S1···S1 = 3.670(3) Å and S1···S4 = 3.543(2) Å), which are a little shorter than the sum of the van der Waals radius, is given at the bottom of the Figure 2a (see ball and sticks chain). Two donors **4** interact through the S1···S1 contacts to form a dimer that interacts through the S2···S2 contacts (Figure 2b).

Compound **10** crystallizes in the monoclinic P2$_1$/n (N°14) space group (Table 1). An ORTEP[23] view of **10** is depicted in Figure 1. The divalent Cu(II) ion is lying in an inversion center and linked to two bischelate hfac$^-$ anions through their oxygen atoms and two ligands **5** through the oxygen atoms of the nitrone group. The Jahn−Teller axis is located in the O4−Cu1−O4′ direction leading to two distances (Cu1−O4 = 2.205(2) Å) longer than the four others Cu−O bond lengths (mean value 1.998(2) Å) (Table 2). The arrangement of the linked ligands endows an elongated octahedral polyhedron around the Cu(II) ion. The coordination angle between the N−O group and the copper center is close to 120° (119.19(15) Table 2), which is smaller than the usual angle observed in monodente-aminoxyl (about 128°),[26] NIT

(24) Cosquer, G.; Pointillart, F.; Le Gal, Y.; Golhen, S.; Cador, O.; Ouahab, L. *Dalton Trans*. **2009**, 3495.
(25) Chahma, M.; Hassan, N.; Alberola, A.; Stoeckli-Evans, H.; Pilkington, M. *Inorg. Chem*. **2007**, *46*, 3807.
(26) (a) Field, L. M.; Lahti, P. M.; Palacio, F. *Chem. Commun*. **2002**, 636. (b) Field, L. M.; Lahti, P. M.; Palacio, F.; Paduan-Fiho, A. *J. Am. Chem. Soc*. **2003**, *125*, 10110. (c) field, L. M.; Lahti, P. M. *Inorg. Chem*. **2003**, *42*, 7447.

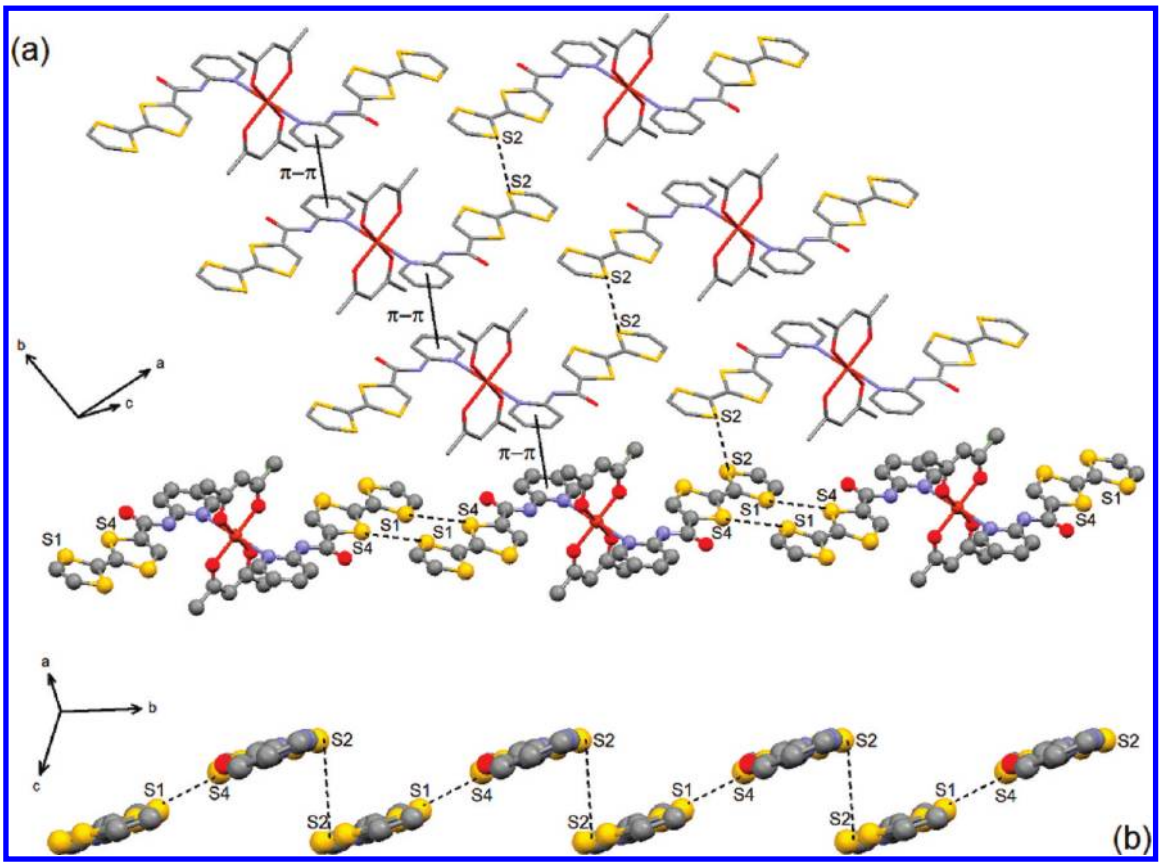

Figure 2. (a) Packing view *trans*-[Cu(hfac)$_2$(**4**)$_2$] (**9**) showing the inorganic and organic networks and highlighting in one hand, the $\pi-\pi$ intermolecular interactions and the short S2···S2 distances along the capped sticks plane [12$\bar{1}$], in the other hand, the short S1···S4 contacts along the ball and sticks chain. (b) Arrangement along the *b*-axis showing all the S···S contacts between the donors.

(nitronyl nitroxide) (about 133°)[27] and TEMPO (*N*-oxyl-2,2,6,6,tetramethyl-piperidine-4-oxyl) (about 166°)[28] adducts of Cu(hfac)$_2$ complexes. In the two first cases, the differences might be explained by the fact that the involving N−O group is a radicaln whereas in the latter one, the four methyl groups of the TEMPO derivative play a crucial role because of their steric hindrance. Both ligands **5** in **10** are not planar. One the one hand, both TTF and pyridine-*N*-oxide are twisted, a good representative torsion angle to show the none-planarity of the ligand **5** in **10** is the angle C5−C6−C7−N1 which is equal to −16.0(4)° compare to −6.2(9)° for **8**, −3.6(9)° for **7**, +1.8(8)° for **9**, and −1.4(7)° for **6**. On the other hand, the TTF group is not planar, as observed in several neutral TTF-based compounds.

The crystal packing of **10** is depicted in Figure 3a. It shows inorganic and organic networks. The inorganic network is composed of Cu(hfac)$_2$ units which are well isolated. The shortest intermolecular distance Cu···Cu is equal to 11.043(3) Å and it is sensibly longer than for other paramagnetic complexes (Table 2). The organic network is composed of donors **5**. The complexes **10** interact through the donors, particularly through short S2···S4 contacts (3.495(2) Å) ,which are shorter than the sum of the van der Waals radius. This is the shortest S···S contact observed in the series of complexes of this work. It is probably due to the original site of coordination of the ligand **5**. In fact, contrary to all the others complexes in which the donors are parallels, in the complex **10**, the donors form an angle of about 120° (Figure 3b), which corresponds to the angle Cu1−N2−O2. The compound **10** is a good illustration of the interplay between the characteristics of the ligands and the solid-state structure. It is certainly a correlation to take into consideration in the aim of multifunctional materials.

Electrochemistry Study. To elaborate efficient molecular precursor for paramagnetic conducting materials, a fundamental point it is to verify the redox-activity of the donors. To satisfy this point, the electrochemistry of all the free donors (**1**−**5**) and complexes (**6**−**12**) are performed.

Redox Properties of the Donors. The redox properties of the donors are determined by cyclic voltammetry and the values of the oxidation potentials are listed in the Table 3. All the donors **1**−**5** have almost the same redox-activity. Two reversible monoelectronic oxidations are observed at about 0.48 and 0.91 V corresponding to the formation of a radical cation and a dication TTF fragment, respectively (see Figure S12 in the Supporting Information). These oxidation potentials are shifted to higher positive values relative to the parent TTF because of partial electron transfer from the donor (TTF) to the acceptor moiety. Moreover, in the case of the donor **5**, the value of the first oxidation wave is a little bit more important with a potential equal to 0.53 V. This shift to

(27) Caneschi, A.; Ferraro, F.; Gatteschi, D.; Rey, P.; Sessoli, R. *Inorg. Chem.* **1991**, *30*, 3162.
(28) Baskett, M.; Lahti, P. M.; Palacio, F. *Polyhedron* **2003**, 2363.

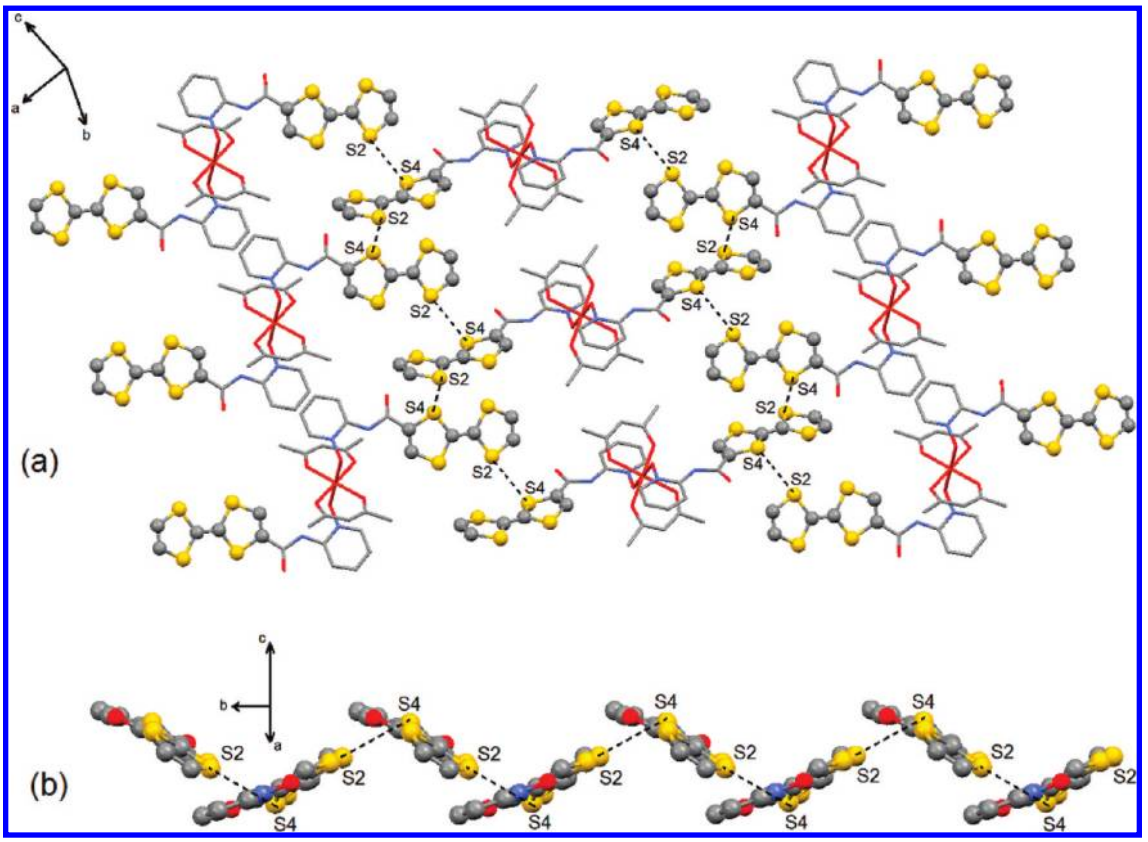

Figure 3. (a) Inorganic and organic networks in *trans*-[Cu(hfac)$_2$(**5**)$_2$] (**10**) with the highlight of the short S2···S4 contacts along the *b*-axis. (b) Arrangement of the donors **5** in complex **10**.

Table 3. Oxidation Potentials (V vs SCE, 0.1 M (n-Bu)$_4$NPF$_6$, in CH_2Cl_2 at 100 mV s^{-1}) of Ligands **1**−**5** and complexes **6**−**12**

	$E^1_{1/2}$	$E^2_{1/2}$
1	0.47	0.90
2	0.46	0.89
3	0.47	0.93
4	0.48	0.91
5	0.53	0.92
6	0.48	0.90
7	0.46	0.93
8	0.48	0.92
9	0.46	0.97
10	0.54	0.93
11	0.51	0.89
12	0.51	0.91

higher positive values compare to the other donors **1**−**4** is due to the stronger acceptor character of the 2-pyridine-*N*-oxide substituent than the other ones (pyrimidine, pyrazine, and pyridine).

The redox properties of the amido-TTF donors can be compared with the most studied family of the amido-EDT-TTF donors.[5f] The oxidation potentials of this family are observed at about 0.70 and 0.92 V, respectively for the formation of the radical cation and dication.[5f,8] The formation of the radical cation TTF fragment is shifted to lower potential of about 0.22 V which permit to obtain a greater accessibility to the partial oxidized and radical form of the donor. No significant modification of the value of the second oxidation wave is observed.

Redox Properties of the Complexes. As observed for the free donors, two reversible monoelectronic oxidations are observed corresponding to the formation of a radical cation and a dication TTF fragment in the complexes, respectively (Table 3 and the Supporting Information, Figure S12). Almost the same oxidation potentials are observed in free and linked donors in the complexes because of the expected weak electronic communication through the not conjugated amido-bridge.[5f]

Table 4. TGA Data for Complexes **6** and **7**

	first weight loss (H_2O for **6**, THF for **7**)			second weight loss (**1** for **6**, **2** for **7**)		
	T (°C)	Exp (%)	Th (%)	*T* (°C)	Exp (%)	Th (%)
6	105−135	2.8	2.2	150−210	39.3	39.6
7	100−150	10.7	11.4	205−290	49.7	51.4

All the complexes have the required redox properties to play the role of molecular precursors for conducting magnets.

Thermal Analyses of 6 and 7. The thermogravimetric analysis of **6** and **7** are realized between 20 and 500 K. The results are given in Figure S13. For both coordinating complexes, two weight losses are observed (Table 4). In the case of **6**, the first weight loss takes place in the range 105−135 °C, corresponding to 2.8% of the total weight. This weight loss corresponds to the starting of the two water molecules of crystallization (Figure S5a) and it is in agreement with the theoretical weight loss value (2.2%). The second weight loss takes place in the range 150−210 °C, corresponding to 39.3% of the total weight. This value corresponds perfectly with the expected value for the decoordination of the two ligands **1**. The second single-step weight loss which occurs in the range 150−210 °C,

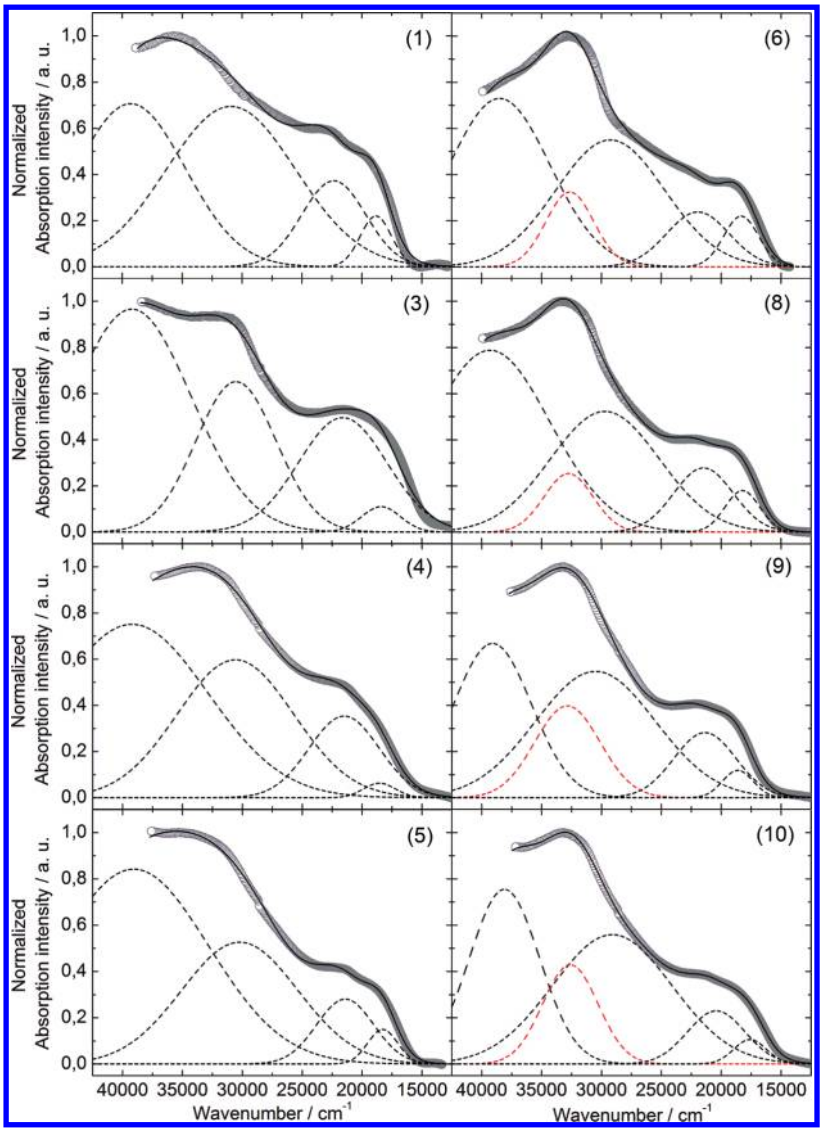

Figure 4. Experimental solid state UV−visible absorption spectra for the ligands **1**, **3**, **4**, **5**, and complexes **6**, **8**, **9**, **10** (open gray circles). Gaussian deconvolutions of the experimental curves are shown in dashed lines and the best fit in full black lines, R = 0.9970, 0.9957, 0.9998, 0.9995, 0.9982, 0.9996, 0.9996, 0.9999, respectively, for **1**, **3**−**6** and **8**−**10**.

indicates that the copper hexafluoroacethylacetonate adducts with ligands **1** is thermally stable up to 150 °C. In the case of **7**, the two weight losses take place in the range 100−150 °C (exp. 10.7%) and 205−290 °C (exp. 49.7%). These two weight losses correspond to the loss of the THF molecules of crystallization (see Figure S5b in the Supporting Information) (th. 11.4%) and the decoordination of the two ligands **2** (th. 51.4%), respectively. The manganese hexafluoroacethylacetonate adducts with ligands **2** is thermally stable up to 205 °C.

The complex **7** is thermally most stable than **6**, probably because of the stronger Lewis base character of donor **2** than of **1**.

EPR Measurements. The X-band EPR spectra of compounds **6**, **7**, **8**, **9**, **10** and **11** have been recorded on microcrystalline samples at liquid nitrogen temperature (see the Supporting Information, respectively, Figures S14−19). The main characteristics of the spectra are the metal centered character of the unpaired electrons, in agreement with previous studies. Specific attention has been paid to the spectra of compounds **9** and **10** for which the Jahn−Teller axes of octahedral Cu(II) are oriented toward the redox-active ligand in **9** and in the $hfac^-$ plane in **10**. The spectrum of **9** can be fairly well reproduced with $g_x = g_y = 2.075$, $g_z = 2.35$, $A_x = 20$ G, $A_y = 35$ G, and $A_z = 135$ G, typical of tetragonally elongated octahedral geometry with hyperfine coupling of a $d_{x^2-y^2}$ unpaired electron with the nuclear spin $I = 3/2$ of Cu. The spectrum of **10** is very similar to the spectrum of **9** with roughly the same hyperfine coupling constant and g factors. The rotation of the Jahn−Teller axis has then no influence on the X-band ESR response.

Photophysical Properties and Theoretical Results. The photophysical properties are determined from absorption solid-state UV−visible spectra. The study is realized with four different free donors (**1**, **3**, **4**, and **5**) and their corresponding complexes (**6**, **8**, **9** and **10**, **11**, **12**). All the UV−visible spectra are performed in the solid state to prevent any dissociation of the complexes and the experimental maximum values are determined by Gaussian deconvolutions of the experimental curves (Figure 4 and the Supporting Information, Figure S20). The shape

Table 5. Experimental UV−Visible Absorption Data for the Ligands **1**, **3**−**5** and Complexes **6**, **8**−**12**

1	3	4	5
18 800	18 400	18 600	18 300
22 300	21 600	21 500	21 400
30 900	30 500	30 600	30 200
39 300	39 200	39 200	39 100

6	8	9	10	11	12
18 300	18 200	18 600	17 600	17 600	17 800
21 900	21 500	21 400	20 400	20 300	20 300
29 300	29 700	30 500	29 100	29 100	29 000
32 600	32 700	32 800	32 600	32 700	32 600
38 500	39 300	39 100	38 100	38 300	38 200

of the experimental absorption spectra of all the donors is quite similar showing two strong absorption bands in the UV spectral region and two bands in the visible region (Figure 4, see Table 5 for numerical values of the maxima). To rationalize the experimental data, a theoretical study is performed (see the computational details). We not only want to assign the bands of the Gaussian deconvolution of the experimental curves but also to quantify the role of the different physical mechanism like the donor−acceptor charge transfers. The computational study has been at first performed, for comparison, on simple molecular systems like the TTF donor and 4-formyltetrathiafulvalene TTF-CHO (see the Supporting Information, Figures S21 and S22 and Tables S2 and S3). The molecular orbital diagrams (Figure 5 and the Supporting Information, Figure S23) and calculated UV−visible spectra (Figure 6 and the Supporting Information, Figure S24) have then been determined for free ligands **1**, **4**, and **5**. Finally a similar work has been performed to determine the first excitation of the complexes **9** and **10** (Figure 7 and the Supporting Information, Figure S25).

With this theoretical calculation, the lowest-energy bands of the absorption spectrum are attributed to $\pi-\pi^*$ charge transfer (CT) corresponding essentially to the HOMO (TTF) → LUMO (A) (A = acceptor) monoelectronic excitation (Table 6, S4, S5 and S6) (The percentage of the transitions composing the excitation corresponds effectively to the square of the coefficients of the transitions and the sum for each excitation must be 100%. Nevertheless, in Table 6, for clarity, only the transitions accounting for at least 10% of the excitation were reported). The HOMO is a π orbital centered on the TTF fragment whereas the LUMO is centered on the acceptor moiety (Figure 5 and the Supporting Information, Figure S23). The lowest-energy transition corresponds therefore to an intramolecular CT from the donor TTF fragment to the acceptor group. That result is in agreement with a previous reported work.[29] It is worthy to note that the theoretical calculations give only one absorption band in the visible (Figure 6 and the Supporting Information, Figure S24) while two bands are experimentally observed (Figure 4). The splitting of the lowest-energy band may be attributed to solid-state effects. State in which the TTF-based ligands are packed and so intermolecular charge transfers might be observed.

(29) Jia, C.; Liu, S.-X.; Tanner, C.; Leiggener, C.; Neels, A.; Sanguinet, L.; Levillain, E.; Leutwyler, S.; Hauser, A.; Decurtins, S. *Chem.—Eur. J.* **2007**, *13*, 3804.

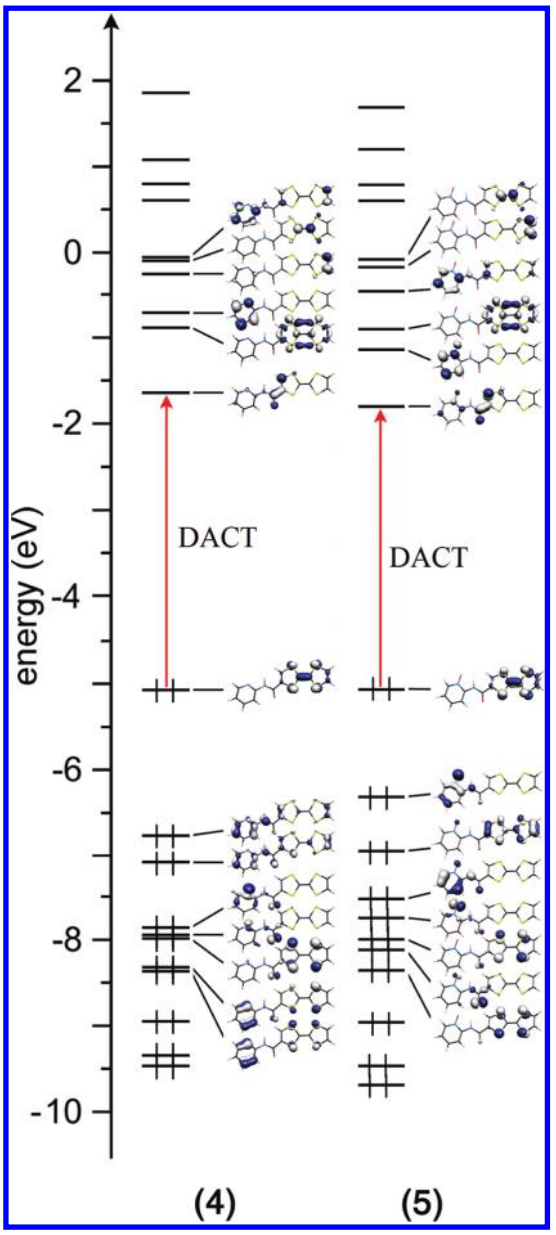

Figure 5. Molecular orbital diagram of compounds **4** and **5**.

In solution, the packing of the molecule can be partially or fully destroyed. In fact, we can notice that, the solution absorption spectrum of **4** shows only one band in the visible region (Left side of the Figure 6). The theoretical energies of the HOMO → LUMO transitions, corresponding to 20 869, 21 354, and 20 434 cm^{-1} respectively for **1**, **4**, and **5**, are consistent with the experimental values found by Gaussian deconvolution (the experimental mean values of the maxima are equal to 20 550, 20 050, and 19 850 respectively for **1**, **4**, and **5**). The energy differences in the series are due to the Lewis base character of the acceptor.

The experimental deconvolution centered between 30 200 and 30 900 cm^{-1} incorporates several intramolecular transitions. For **1**, the large absorption band centered at 30 900 cm^{-1} is composed of the $\pi-\pi^*$ intraligand HOMO-1 (L) → LUMO (pym) transition (L = whole molecule) and $\pi-\sigma^*/\pi^*$ intra-TTF transitions (HOMO (TTF) → LUMO+5/+6/+7 (TTF), HOMO (TTF) → LUMO+5/+6 (TTF) and

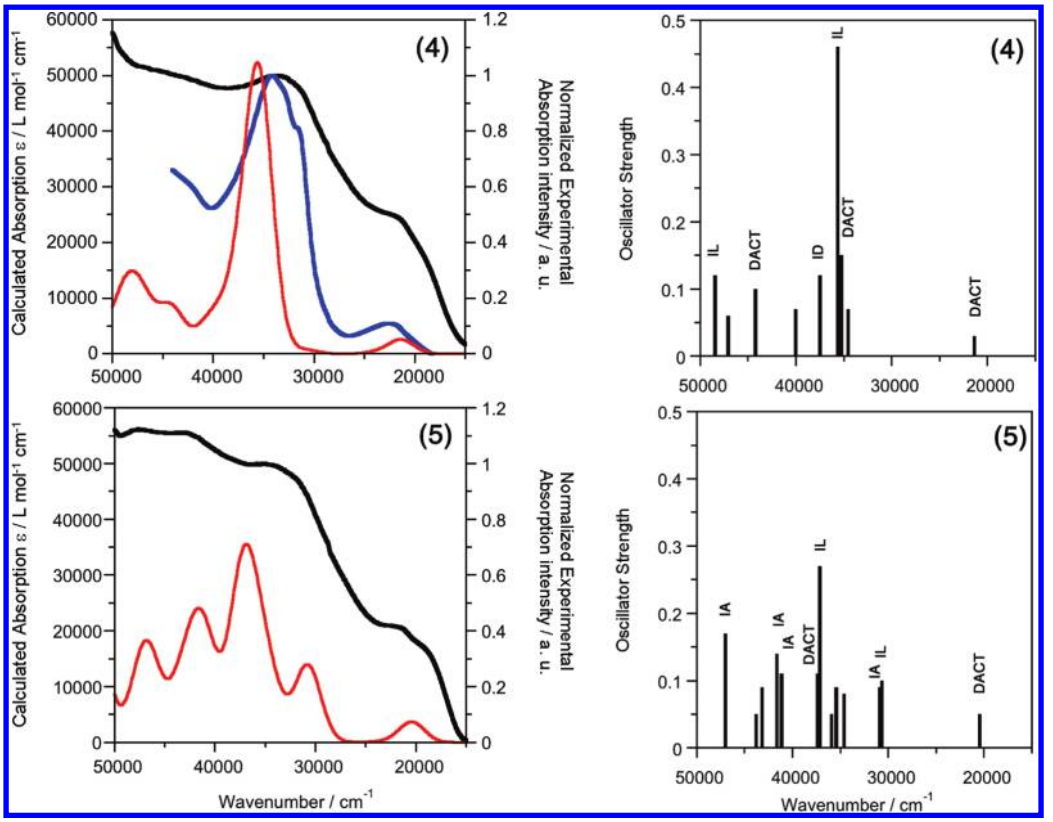

Figure 6. On the left side, theoretical and experimental absorption spectra of compounds **4** and **5**. Solid-state and solution measurements correspond respectively to black and blue lines while the red correspond to calculated spectra with an optimized geometry. On the right side, selected most pertinent low-lying electronic transitions and assignment of compounds **4** and **5**.

Table 6. Most Important TD-DFT Calculated Excitations Energies Associated with an Oscillator Strength $f > 0.10$ (except for the lowest excitation) and Assignment of Low-Lying Electronic Transitions (with participation ≥10%) of **1**, **4**, and **5**[a]

	energy exp (cm^{-1})	energy th (cm^{-1})	osc.	type	assignment	transition
1	20 550	20 869	0.03	DACT	$\pi^{nb}_{TTF} \rightarrow \pi^*_{pym}$	Ho → Lu (91%)
	30 900	34 678	0.10	ID	$\pi^{nb}_{TTF} \rightarrow \sigma^*/\pi^*_{TTF}$	Ho → Lu + 5/+6/+7 (63%)
						Ho-1 → Lu+2 (17%)
		35 760	0.35	IL	$\pi_L \rightarrow \pi^*_{pym}$	Ho-1 → Lu (72%)
		36 141	0.21	ID	$\pi^{nb}_{TTF} \rightarrow \sigma^*/\pi^*_{TTF}$	Ho → Lu+5/+6 (75%)
	39 300	46 818	0.11	IL	$\pi_L/n_S \rightarrow \pi^*_L/\sigma^*_{TTF}$	Ho-1 → Lu+3 (52%)
						Ho-4 → Lu+2 (23%)
		48 500	0.09	IL	$\pi_L \rightarrow \pi^*_L$	Ho-1→ Lu+3/+4 (55%)
						Ho-3→ Lu+3 (19%)
4	20 050	21 354	0.03	DACT	$\pi^{nb}_{TTF} \rightarrow \pi^*_{pyN}$	Ho → Lu (90%)
	30 600	35 259	0.15	DACT	$\pi^{nb}_{TTF} \rightarrow \pi^*_L$	Ho → Lu+5/+6 (75%)
		35 627	0.46	IL	$\pi_L \rightarrow \pi^*_{pyN}$	Ho-1→Lu (83%)
		37 500	0.12	ID	$\pi^{nb}_{TTF} \rightarrow \sigma^*/\pi^*_{TTF}$	Ho → Lu+4/+7 (67%)
	39 200	44 214	0.10	DACT	$\pi_{TTF}/n_S \rightarrow \pi^*_{pyN}$	Ho-5/-4 → Lu (71%)
		48 433	0.12	IL	$\pi_L/n_S \rightarrow \pi^*_L$	Ho-7/-6 → Lu (33%)
						Ho-2 → Lu+3 (12%)
5	19 850	20 434	0.05	DACT	$\pi^{nb}_{TTF} \rightarrow \pi^*_{pyNO}$	Ho → Lu (91%)
	30 200	30 676	0.10	IL	$\pi^{nb}/\pi_L \rightarrow \pi^*_L$	Ho → Lu+3/+4 (62%)
						Ho-1 → Lu (24%)
		30 857	0.09	IA	$\pi_{pyNO} \rightarrow \pi^*_{pyNO}$	Ho-1 → Lu (61%), Ho → Lu+3/+4 (23%)
		37 150	0.27	IL	$\pi^{nb}/\pi_L \rightarrow \sigma^*/\pi^*_L$	Ho → Lu+5/+7 (37%)
						Ho-2 → Lu (20%)
						Ho-1 → Lu+1 (10%)
		37 409	0.11	DACT	$\pi^{nb}/\pi_{TTF} \rightarrow \sigma^*_{TTF}/\pi^*_L$	Ho → Lu+5/+7 (45%)
						Ho-2 → Lu (28%)
	39 100	41 135	0.11	IA	$\pi_{pyNO} \rightarrow \pi^*_{pyNO}$	Ho-1 → Lu+3 (42%)
						Ho-3 → Lu (27%)
		41 614	0.14	IA	$\pi_{pyNO} \rightarrow \pi^*_{pyNO}$	Ho-3 → Lu (37%)
						Ho-1 → Lu+1/+3 (37%)
		46 986	0.17	IA	$\pi_{pyNO} \rightarrow \pi^*_{pyNO}$	Ho-3 → Lu+1 (58%)
						Ho-1 → Lu+4 (10%)

[a] D, A, L, Ho, Lu, nb, and nS represent, respectively, TTF (donor), pyNO (acceptor), whole molecule, HOMO, LUMO, non-bonding orbital, and the molecular orbitals where the lone pair character is predominant; therefore, DACT stands for donor to acceptor charge transfer and ID for intradonor.

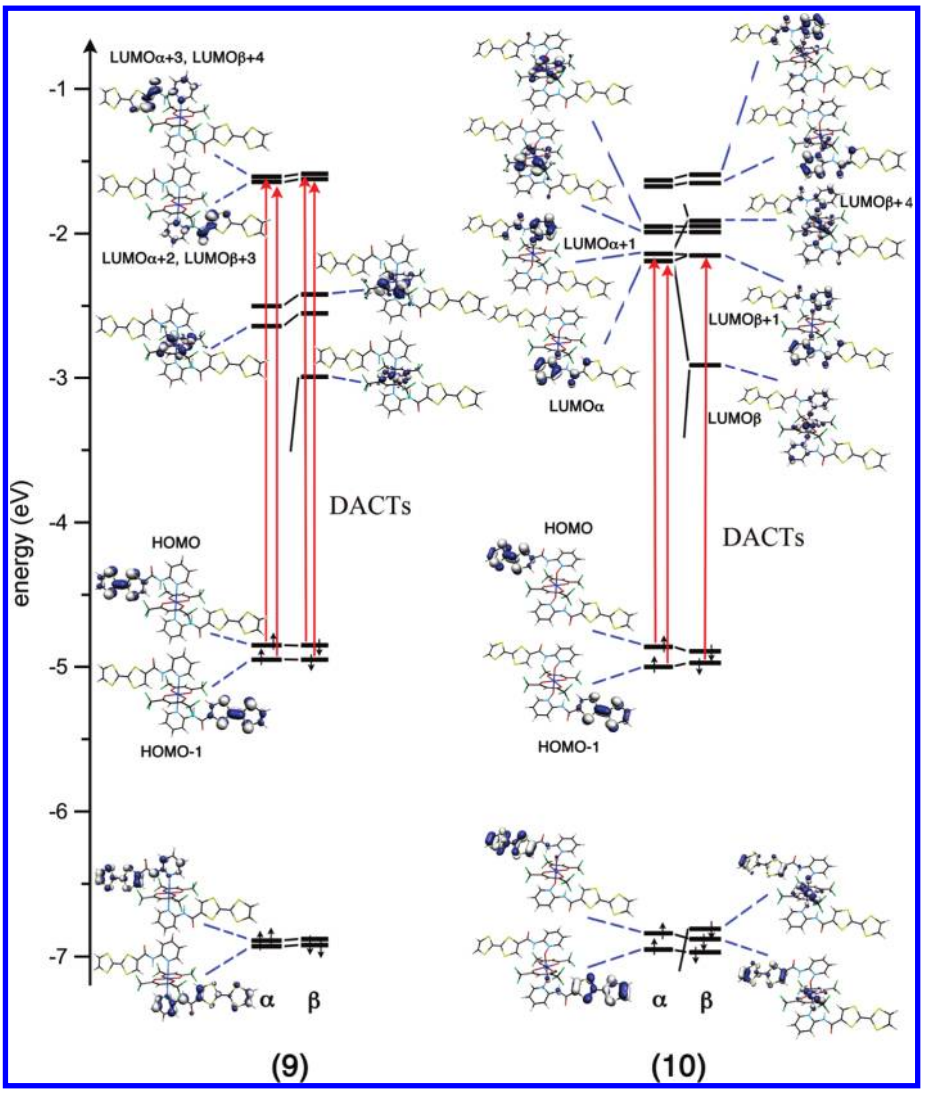

Figure 7. Molecular orbital diagram of compounds **9** and **10**.

HOMO(TTF) → LUMO+5/+7 (TTF)) (see the Supporting Information, Figures S4 and S24 and Table 6). The σ contributions in those intra-TTF transitions is due to overlap between π and σ^* centered TTF orbitals coming from the deviation to the planar conformation of the TTF fragment. For **4**, the molecular orbitals are more mixed between TTF fragment and acceptor than for **1**. The principal contribution of the deconvolution at 30600 cm^{-1} comes from the $\pi-\pi^*$ intraligand HOMO-1 (L) → LUMO (Py) transition. Two other significant contributions have been identified, the charge transfers (HOMO (TTF) → LUMO+5/+6 (Py)) and $\pi-\sigma^*/\pi^*$ intra-TTF transitions (HOMO (TTF) → LUMO+4/+7 (TTF)) (right side of Figure 6, Table 6, and the Supporting Information, Table S5). Finally for **5**, the pyridine-*N*-oxide moiety is the strongest Lewis base of the series (as demonstrated by the electrochemical properties) and the molecular orbitals are found well localized in the TTF or acceptor fragments (Figure 5). The principal contributions of the deconvolution at 30200 cm^{-1} comes from $\pi-\sigma^*/\pi^*$ intraligand transitions and TTF-PyNO (where PyNO = 2-pyridine-*N*-oxide) charge transfers. These latter excitations are given by the combination of different ratio of the following transitions: HOMO (TTF) → LUMO+5 (TTF), HOMO-2 (TTF) → LUMO (PyNO) and HOMO (TTF) → LUMO+7 (TTF) (Table 6 and the Supporting Information, Table S6). The deconvolution localized at 30200 cm^{-1} includes also two others $\pi-\pi^*$ intraligand and intra-PyNO contributions. These $\pi-\pi^*$ electronic transitions are described by different ratios of the following excitations: HOMO (TTF) → LUMO+3 (PyNO), HOMO (TTF) → LUMO+4 (TTF) and HOMO-1 (PyNO) → LUMO (PyNO) (Table 6 and the Supporting Information, Table S6).

The experimental deconvolution centered between 39 100 and 39 300 cm^{-1} incorporates few intramolecular transitions that are identified. The nature of these transitions depends of the Lewis base character of the acceptor moiety. For **1**, electronic intraligand excitations are described by the HOMO-1 (L) → LUMO+3 (PyNO), HOMO-4 (TTF) → LUMO+2 (TTF), HOMO-1 (L) → LUMO+4 (TTF), and HOMO-3 (Pym) → LUMO+3 (Pym) transitions (Table 6 and the Supporting Information, Table S4). When the acceptor moiety is a pyridine (for **4**), the deconvolution can be described by the combination of $\pi-\pi^*$ charge transfers (HOMO-5 (TTF) → LUMO (Py) (60%) and HOMO-4 (Py) → LUMO (Py) (11%)) and $\pi-\pi^*$ intraligand transitions (HOMO-6/-7 (L) → LUMO (Py) and HOMO-2 (L) → LUMO+3

Table 7. First Pertinent TD-DFT Calculated Excitations Energies Associated with an Oscillator Strength $f > 0.01$ and Assignment of Low-Lying Electronic Transitions (with participation ≥10%) of Compounds **9** and **10**[a]

complexes	energy (cm^{-1})	λ (nm)	osc.	type	assignment	transition
9	19735	507	0.11	DACT	$\pi^{nb}{}_{TTF} \rightarrow \pi^{*}{}_{py}$	Hoα-1 → Luα+2 (23%) Hoα → Luα+3 (22%) Hoβ-1 → Luβ+3 (23%) Hoβ → Luβ+4 (22%)
10	17965	557	0.11	DACT	$\pi^{nb}{}_{TTF} \rightarrow \pi^{*}{}_{pyNO}$	Hoβ-1 → Luβ+1 (30%) Hoα-1 → Luα (11%) Hoα → Luα (10%) Hoα → Luα+1 (11%) Hoβ → Luβ+2 (10%)

[a] DACT stands for donor to acceptor charge transfer and Ho and Lu represent respectively, the HOMO and LUMO.

(TTF)) (Table 6 and the Supporting Information, Table S5). Finally, when the acceptor is a strong Lewis base as the 2-pyridine-*N*-oxide (for **5**), the highest energy deconvolution is described with intra-acceptor transitions (HOMO-1 (PyNO) → LUMO+1/+3 (PyNO) and HOMO-3 (PyNO) → LUMO+0/+1 (PyNO)) (Table 6 and the Supporting Information, Table S6).

In a second step, this theoretical approach has been performed on two representative complexes showing two different behaviors toward the complexation effect.

The UV−visible spectra of complexes **9** and **10** are depicted in Figure 4. The shape of these spectra is similar to those for free ligands. An additional absorption band is observed around 32700 cm^{-1} (red deconvolution) due to the intramolecular $\pi-\pi^*$ charge transfer of the $hfac^-$ anions. A red shift of the absorption bands is observed for **10** because of the coordination of the metallic precursor $Cu(hfac)_2$, whereas the shift is negligible for **9**. The lowest and highest-energy bands are respectively red-shifted to 800 and 1000 cm^{-1}. The coordination of a metal ion to the substituent site reduces the electronic density on the aromatic ring system and induces a new localization of the molecular orbitals, leading respectively to the energy increase in the π orbital and energy decrease in the π^* orbitals. The energy stabilization is more important in **10** than in **9** due to the orientation of the Jahn−Teller axis. In fact, in **10**, the Cu1−O2 distances are short (1.981(2)Å) and the electronic effect of the coordination is strong while in **9**, the Cu1−N2 distances are long (2.431(4) Å) and the electronic effect of the coordination is weak. The electronic effect of the coordination is principally an electrostatic effect because the red shift of the $\pi-\pi^*$ monoelectronic excitations are almost the same for the coordination of $Cu(hfac)_2$ (for **10**), $Mn(hfac)_2$ (for **11**) and $Zn(hfac)_2$ (for **12**) (see the Supporting Information, Figure S20). The molecular spinorbital diagrams of the compounds **9** and **10** were determined and shown in Figure 7. Theoretical composition according to a Mulliken population analysis of the frontier spinorbitals of the solid-state structure of **9** and **10** are given in the Supporting Information, Tables S7 and S8. The calculated electronic excitations manage to reproduce the first absorption band (see the Supporting Information, Figure S25). The monoelectronic transitions responsible for this absorption band are represented in the molecular spinorbital diagram (Figure 7). For the complex **9**, the absorption band centered at 19735 cm^{-1} (excellent agreement with the experimental value of 20000 cm^{-1}) is due to an excited state composed of the HOMOα-1 (TTF) → LUMOα+2 (Py), HOMOα (TTF) → LUMOα+3 (Py), HOMOα-1 (TTF) → LUMO α+3 (Py) and HOMOα (TTF) → LUMO α+4 (Py). All the transitions have similar contributions due to the quasi degeneration of the HOMO, HOMO-1, LUMO+2 and LUMO+3 spinorbitals (Figure 7, Table 7). These electronic transitions are described as intramolecular $\pi-\pi^*$ charge transfers from the TTF to amido-pyridine fragment. In other words, the absorption band centered at 19735 cm^{-1} can be compared to the HOMO → LUMO transition of the coordinated ligand **4** in the complex **9**. This excitation has a lower energy (−1619 cm^{-1}) compared to the calculated equivalent excitation for the free ligand **4** (21354 cm^{-1}). The theoretical molecular oribtals diagrams show that the decrease of the energy of this excitation is due to a destabilization of the bonding orbitals (0.24 eV), whereas the antibonding orbitals remain almost unchanged (see the Supporting Information, Figure S26). Experimentally, the energy difference was found to be negligible between the free and coordinated ligand (−50 cm^{-1}) (Table 5). The second studied case concern the complex **10**; the absorption band centered at 17965 cm^{-1} (in agreement with the experimental value of 19000 cm^{-1}) is due to an excited state composed of the HOMOβ-1 (TTF) → LUMO β+1 (PyNO), HOMOα-1 (TTF) → LUMOα (PyNO), HOMOα (TTF) → LUMOα (PyNO), HOMOα (TTF) → LUMOα+1 (PyNO), and HOMOβ (TTF) → LUMOβ+2 (PyNO) (Table 7). The Jahn−Teller axis in **10** is now in the plane formed by the two $hfac^-$ ligands and the crucial consequence is a mixing between the orbitals of the ligand and the metal center (see the LUMOβ and LUMO β+4 orbitals). In other terms, when ligand **5** is used, some ligand−metal charge transfers occur. The HOMO → LUMO energy excitation of the coordinated ligand **5** is now much lower (−2469 cm^{-1}) than for free ligand (20434 cm^{-1}). The energy decrease of the HOMO → LUMO excitation of fragment **5** in complex **10**, is due to simultaneous destabilization of the bonding orbitals (0.22 eV) and stabilization of the antibonding orbitals (−0.4 eV) (Figure S23). Experimentally, the energy difference was found equal to −850 cm^{-1} between the free and the coordinated ligand (Table 5). The theoretical calculations demonstrate that the effect of the coordination of the Cu(II) is stronger in **10** than in **9** and confirm the experimental observations.

The spin density distributions for compounds **9** and **10** are depicted in Figure 8. They represent the localization of the unpaired electron of the formally Cu(II) cations. The Jahn−Teller deformation breaks the degeneracy of

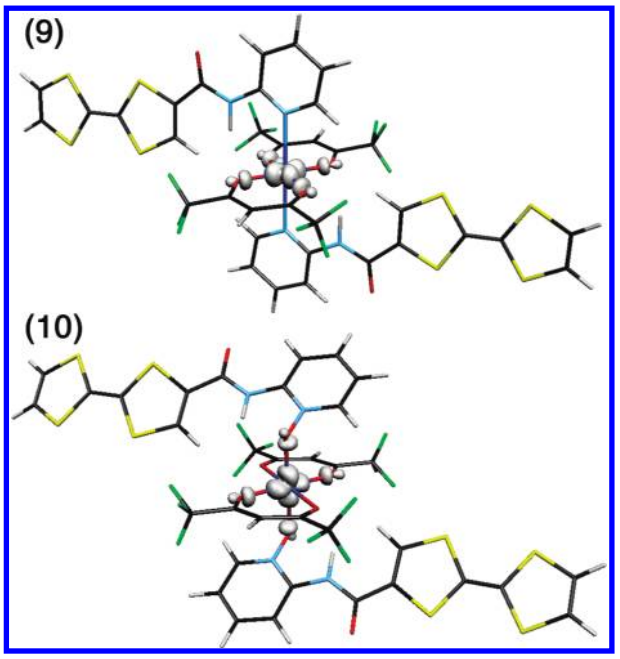

Figure 8. Spin density distribution for compounds **9** and **10** corresponding to the $S = 1/2$ ground state. The isodensity surface represented corresponds to a value of 0.01 $e^-/bohr^3$ (positive values are represented as white surfaces and no negative values were observed).

the e_g type metal−ligand antibonding orbitals, therefore the two long distances will be associated to a d_{z^2} orbital with paired electrons and the unpaired electron is found in a $d_{x^2-y^2}$ type orbital. Thus, we observe that for **9**, the spin density is confined in the plane formed by the two $hfac^-$ ligands, whereas for **10**, it is localized along the $Cu-O_{Ligand}$ direction and along one of the two arms of the $hfac^-$ ligands. This simple evaluation of the greater implication of the Cu(II) unpaired electron in the π orbitals of the acceptor corroborates the greater shift seen in the complex **10**.

Conclusions

In the present work, five new amido-TTF ligands and seven coordination complexes have been synthesized and discussed in both experimental and theoretical point of views. All the complexes have been crystallized and their crystal structure determined. The influence of the acceptor nature on the crystal organization has been investigated. The cyclic voltammetry attested the redox active behavior of the free and coordinated donors, nevertheless the comparison between the electrochemical properties of the TTF derivatives and complexes does not permit us to study the coordination effect of the divalent metal. To realize such a study, all the compounds have been investigated by solid-state UV−visible absorption spectroscopy. Gaussian deconvolutions of the experimental curves were performed to fit the data. The molecular orbital diagrams for **4** and **5** donors and their corresponding complexes have been elaborated and TD-DFT calculations have permitted to reproduce the absorption spectra. The low energy transitions are identified as monoelectronic HOMO → LUMO charge transfers from donor fragment to acceptor moiety, whereas the high-energy region is composed of intraligand $\pi-\pi^*$ excitations. It was demonstrated that the Lewis base character of the acceptor influences the nature of the high energy $\pi-\pi^*$ transitions. The absorption transitions are red-shifted in the coordination complexes compared to the free amido-TTF derivatives. The comparison of photophysical properties of the isostructural complexes *trans*-[$M(hfac)_2(\mathbf{5})_2$] (M = Cu, Mn and Zn) has shown no difference for the maxima values of the absorption bands highlighting the electrostatic character of the coordination effect. Finally, the experimental and theoretical investigations have demonstrated the drastic influence of the Jahn−Teller deformation of the Cu(II) ion. For *trans*-[$Cu(hfac)_2(\mathbf{4})_2$], the coordination effect is weak because of the elongation along the N−Cu−N direction, whereas it is strong for *trans*-[$Cu(hfac)_2(\mathbf{5})_2$] because of the reorientation of the Jahn−Teller axis in the plane formed by the $hfac^-$ anions. It has been shown in this complex that a strong coordination of the donors leads to a mixing of the ligand and metallic orbitals because of the ligand−metal charge transfers. Such transitions are very promising to obtain interesting optical materials and the use of the ligand **5** with lanthanide ions is under investigation in our group.

Acknowledgment. This work was supported by the CNRS, MAGMANet European excellence network, Université de Rennes 1, and la Région Bretagne.

Supporting Information Available: CIF files for **1**, **6**−**12**; full structural descriptions of **6**−**8** and **11**−**12** (Table S1 and Figure S1−11); the cyclic voltammograms of the ligands **1**−**6** and complexes **7**−**12** (Figure S12); thermal analysis for complexes **6** and **7** (Figure S13); EPR spectra for complexes **6**-**11** (Figure S14−S19); solid-state UV−visible absorption spectra for **10**, **11**, and **12** (Figure S20); molecular orbital diagram of compounds TTF, TTF-CHO, **1**, **4**, and **5** (Figure S21); theoretical and experimental absorption spectra of TTF and TTF-CHO (Figure S22); molecular orbital diagram of ligand **1** (Figure S23); theoretical and experimental absorption spectra of compounds **1** (Figure S24); theoretical and experimental absorption spectra of compounds **9** and **10** (Figure S25); molecular orbital diagram of ligands **4**, **5**, and their corresponding complexes **9** and **10** (Figure S26); TD-DFT data for TTF, TTF-CHO, **1**, **4**, and **5** (Table S2−S6, respectively); theoretical composition according to a Mulliken population analysis of the frontier spinorbitals of the solid-state structure of **9** and **10** (Tables S7, S8); relaxed coordination of TTF, TTF-CHO, **1**, **4**, and **5** with a PBE1 functional and double-ζ quality basis (PDF). This material is available free of charge via the Internet at http://pubs.acs.org.